Electronic and structural response to pressure in the hyperkagome-lattice Na_{3}Ir_{3}O_{8}

F. Sun, H. Zheng, Y. Liu, E. D. Sandoval, C. Xu, J. Xu, C. Q. Jin, C. J. Sun, W. G. Yang, H. K. Mao, J. F. Mitchell, A. N. Kolmogorov, and D. Haskel

Phys. Rev. B **98**, 085131 — Published 20 August 2018

DOI: 10.1103/PhysRevB.98.085131

Electronic and structural response to pressure in hyper-kagome lattice $Na_3Ir_3O_8$

F. Sun,[1,2,3] H. Zheng,[4] Y. Liu,[3,5] E. D. Sandoval,[6] C. Xu,[1] J. Xu,[4,7] C. Q. Jin,[3,8] C. J. Sun,[2] W. G. Yang,[1,9] H. K. Mao,[1,9] J. F. Mitchell,[4] A. N. Kolmogorov,[6,*] and D. Haskel[2,†]

[1]*Center for High Pressure Science and Technology Advanced Research (HPSTAR), Beijing 100094, China*
[2]*Advanced Photon Source, Argonne National Laboratory, Argonne, Illinois 60439, USA*
[3]*Beijing National Laboratory for Condensed Matter Physics and Institute of Physics, Chinese Academy of Sciences, Beijing 100190, China*
[4]*Materials Science Division, Argonne National Laboratory, Argonne IL 60439, USA*
[5]*Xi'an Modern Chemistry research Institute, Xi'an 710065, China*
[6]*Department of Physics, Applied Physics and Astronomy, Binghamton University, State University of New York, Binghamton, New York 13902-6000, USA*
[7]*Physics Department, Northern Illinois University, Dekalb, Illinois 60115*
[8]*Collaborative Innovation Center of Quantum Matter, Beijing 100871, China*
[9]*High Pressure Synergetic Consortium (HPSynC), Geophysical Laboratory, Carnegie Institution of Washington, Argonne, Illinois 60439, USA*

The hyper-kagome lattice iridate $Na_3Ir_3O_8$, closely related to spin liquid candidate $Na_4Ir_3O_8$, is unusual in that spin-orbit interactions acting on the 1/3-filled $J_{\rm eff} = 1/2$ state lead to a semimetallic ground state, in contrast to the conventional insulating Mott state stabilized by S-O interactions in the 1/2-filled $J_{\rm eff} = 1/2$ state of other iridates including $Na_4Ir_3O_8$. We have studied the evolution of crystal structure, electronic structure, and transport in $Na_3Ir_3O_8$ under high pressure using x-ray diffraction, x-ray absorption near edge structure, and electrical resistance measurements in a diamond anvil cell. The study was augmented by the use of *ab initio* calculations which provided insight into pressure-induced changes in crystal and electronic structure. We found that $Na_3Ir_3O_8$ transforms from a semimetal to an insulator under pressure, with an estimated energy gap that increases to about 130 meV at $P \sim 9$ GPa. At approximately 10 GPa a cubic-to-monoclinic structural transition takes place between two insulating phases. This structural transition features a sizable volume collapse and a high-pressure phase characterized by apparent dimerization of Ir-Ir distances, wide dispersion of Ir-O-Ir bond angles, and an increase in the occupation of $5d$ states. Although the energy gap is reduced in the high-pressure phase, insulating behavior remains to the highest pressures ~ 1 Mbar. The strongly pressure-dependent insulating gap shows a positive correlation with the expectation value of the angular part of the S-O interaction, $\langle \mathbf{L} \cdot \mathbf{S} \rangle$, which may indicate an active role of S-O interactions in stabilizing the insulating state that emerges in the compressed $Na_3Ir_3O_8$ structure.

I. INTRODUCTION

Intricate correlations among orbital, spin, and lattice degrees of freedom in transition metal oxides lead to unique quantum states[1–13]. Recent attention has focused on heavy ion $5d$ systems with partially filled t_{2g} levels where strong spin-orbit coupling (SOC) leads to entanglement of spin and orbital degrees of freedom[14–16]. Examples based on iridium ions (primarily in 4+ oxidation state) include the Ruddlesden-Popper phase Sr_2IrO_4 with spin-orbit Mott state[17,18], geometrically frustrated magnets in proximity to a Kitaev spin liquid state such as the 2D (3D) honeycomb (hyperhoneycomb) lattices of α (β, γ) (Li, Na)$_2IrO_3$[19,20], and the frustrated hyper-kagome lattice of $Na_4Ir_3O_8$[21]. The latter, featuring a corner-sharing triangular network of Ir $J_{\rm eff} = 1/2$ moments, is a Mott insulator[21]. The strong SOC acting on iridium's partially filled $5d$ levels lifts the orbital degeneracy. The combined effects of SOC, intersite hopping t, onsite Coulomb repulsion U, and crystal field interaction Δ are responsible for the $J_{\rm eff} = 1/2$ Mott state. The delicate balance among these interactions appears to be essential for these novel quantum ground states, which are absent without SOC[22]. Recent muon spin relaxation (μSR) experiments point toward an unusual magnetic ground state in $Na_4Ir_3O_8$, with emergence of short-range correlations instead of the intrinsically dynamic quantum ground state characteristic of a spin liquid[23].

Iridium oxide $Na_3Ir_3O_8$ shares the same Ir-O hyper-kagome network as $Na_4Ir_3O_8$ but Ir ions formally take a nominal valence of 4.33+ as opposed to 4+. Therefore, Na-deficient $Na_3Ir_3O_8$ can be viewed as a 1/3 hole-doped hyper-kagome spin liquid candidate[23,24]. In contrast to $Na_4Ir_3O_8$, $Na_3Ir_3O_8$ is a paramagnetic semimetal with the unusual effect that SOC acting on t_{2g}-derived molecular orbitals on Ir triangles leads to the gap closure[24]. Like doping, external pressure is expected to modify the electronic properties of these hyper-kagome materials by way of tuning interatomic distances and crystal structure and related changes in electronic hopping integrals, on-site correlations, crystal field interactions, band filling, and strength of effective SOC associated with $5d$-derived bands or molecular orbitals. A number of recent studies highlight the extreme tunability of the delicately balanced interactions in iridates to external pressure[25–33].

In this paper, we have used x-ray absorption near edge structure (XANES), x-ray diffraction (XRD) and electrical resistance measurements in the diamond anvil cell, together with *ab initio* calculations of $Na_3Ir_3O_8$ at high pressures, to unravel a profound interplay be-

tween the electronic and structural degrees of freedom. A transition from a semimetallic to an insulating state takes place below about 2 GPa. With increasing pressure, the electronic gap increases and reaches an estimated maximum value of 130 meV at $P \sim 9$ GPa. However, a first-order structural transition at this pressure strongly renormalizes the insulating gap which decreases but remains open to the highest pressure $P \sim 1$ Mbar. Structure prediction from *ab initio* calculations enabled a more robust interpretation of the XRD data and determination of the high pressure phase symmetry as monoclinic $P2_1$ structure. This low-symmetry structure adopts a distorted Ir framework featuring remarkably short Ir-Ir distances consistent with Ir dimerization. This strong reduction in Ir-Ir distance is likely responsible for the decrease in the size of the electronic gap above the structural transition. A wide distribution of Ir-O-Ir angles in the high-pressure phase, coupled with an increase in the $5d$ occupation under pressure which moves the system towards half-filling, may act to increase electron correlations and reduce inter-site hopping preventing full gap closure at the highest measured pressure.

II. EXPERIMENTAL AND THEORETICAL METHODS

A. Sample synthesis and characterization

$Na_3Ir_3O_8$ crystals were grown by a vapor transport method simultaneously with the growth of $Na_4Ir_3O_8$ crystals, as discussed in Ref.[34]. This growth process yielded crystals with two distinct morphologies: rhombic dodecahedral and hexagonal plate-like. The latter were always found to correspond to the honeycomb lattice compound Na_2IrO_3. The rhombic dodecahedral crystals were assiduously characterized with energy dispersive x-ray (EDX) analysis, magnetization and crystallography to convincingly establish that the $Na_3Ir_3O_8$ samples used in the current work are consistent with the structural, magnetic and transport properties reported in Ref.[24], for which crystals of $Na_3Ir_3O_8$ composition were grown from a flux. Magnetic susceptibility measurements were performed on single crystals using a Quantum Design MPMS-3 SQUID magnetometer. Four-probe electrical resistivity measurements were carried out on a single crystal at ambient pressure in the 2-300 K temperature range using a Quantum Design PPMS system.

B. High pressure x-ray absorption near edge structure and powder x-ray diffraction

The x-ray absorption near edge structure (XANES) measurements were carried out at beamline 4-ID-D of the Advanced Photon Source (APS), Argonne National Laboratory across the Ir $L_{2,3}$ absorption edges ($2p_{1/2,3/2} \rightarrow 5d$ transition). A single crystal sample was finely ground into powder before the experiments. High pressure XAS data was collected using a Princeton Symmetric Diamond Anvil Cell (DAC) with 180 μm beveled culet anvils. To minimize x-ray absorption in the diamond anvils, a partially perforated anvil (0.15 mm remaining thickness) was used opposite a mini-anvil (0.8 mm height) mounted on a fully perforated anvil[35]. A rhenium gasket was pre-indented and a sample chamber laser-drilled with a diameter of 90 μm. Powder was loaded into the sample chamber together with ruby balls as pressure marker. Neon was used as pressure transmitting medium, leading to a reduction of sample chamber diameter to 70 μm. High pressure powder XRD measurements were performed at beamline 16 BM-D of APS, using a Mao-Bell symmetric cell with 300 μm diamond anvil culets. Powder sample was loaded with neon as pressure transmitting medium and ruby balls as pressure marker. The x-ray wavelength was 0.3263 Å and XRD patterns were collected with a MAR 3450 image plate detector.

C. High pressure electrical transport measurements

The resistance measurements under pressure were carried out using the standard four-probe method using slim gold wires as electrodes. A CuBe DAC featuring beveled diamonds with 100 μm culet size was used in a Maglab system, a thermometer located near one of the diamonds serving as temperature monitor.[36]. A hole with diameter of 110 μm was laser-drilled in the center of a pre-indented T301 stainless steel gasket. Cubic boron nitride (cBN) fine powder was used as the insulating layer between the metallic gasket and the electrode leads. The cBN powder was indented and further drilled into a sample chamber with a diameter of 60 μm. A single crystal with approximate dimensions 30 μm$\times$ 40 μm$\times$ 15 μm was loaded into this chamber with soft NaCl fine powder as the pressure transmitting medium. Pressure calibration was determined via the ruby fluorescence method below around 40 GPa, and diamond vibron Raman measurements above 40 GPa.

D. Theory: Structure search and band structure calculation

All simulations were carried out at the density functional theory (DFT) level with VASP.[37,38] We employed projector augmented wave (PAW) potentials[39] and Perdew-Burke-Ernzerhof (PBE) exchange-correlation[40] functional in the generalized gradient approximation.[41] A 500 eV energy cutoff and at least 4×4×4 Monkhorst-Pack k-meshes[42,43] ensured good numerical convergence. The residual atomic forces and the differences from the targeted stress values were below 0.005 eV/Å and 1 kB, respectively. We used the evolutionary algorithm in the MAISE package to search for the ground states of $Na_3Ir_3O_8$ at 15 and 20 GPa using a standard combi-

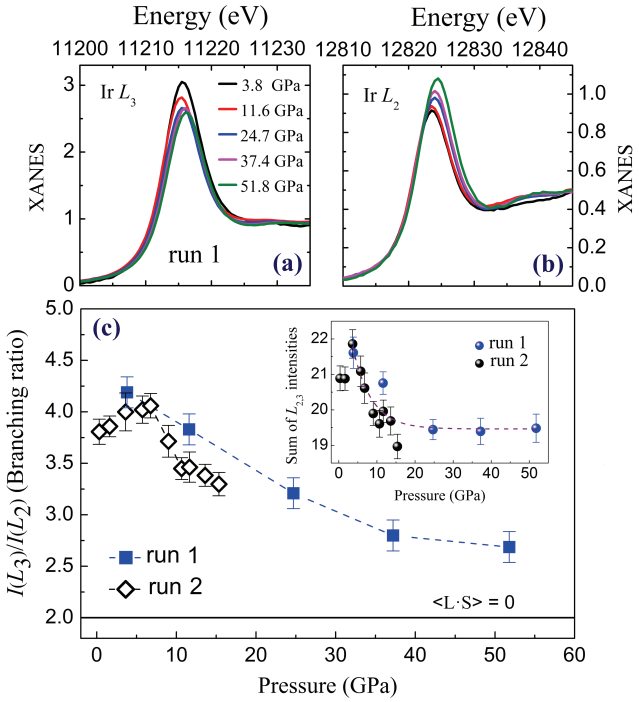

FIG. 1: (a), (b) Ir $L_{2,3}$ XANES data at $T = 300$ K as a function of pressure to over 50 GPa collected in experimental run 1. (c) Pressure dependence of the derived branching ratio at $T = 300$ K measured in independent experiments (run 1 and run 2). The inset shows the pressure dependence of the sum of $L_{2,3}$ intensity in isotropic spectra for two independent experimental runs. The dashed line is guide to the eye.

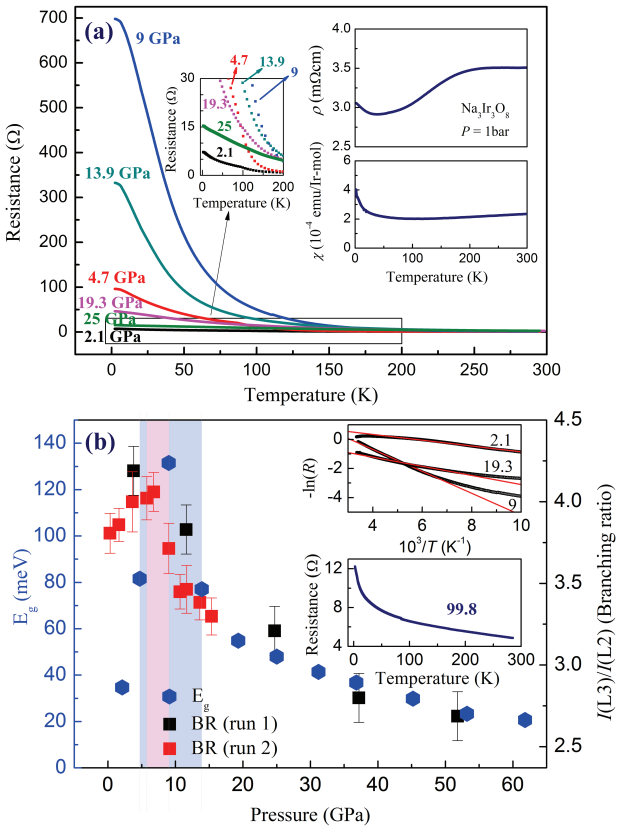

FIG. 2: (a) Temperature dependence of the resistance at various pressures for $Na_3Ir_3O_8$. The details of the resistance below 30 Ω has been enlarged and displayed above. The inset shows the resistivity and magnetic susceptibility of $Na_3Ir_3O_8$ single crystal at ambient pressure. (b) Estimates of the pressure-dependent insulating gap of $Na_3Ir_3O_8$ obtained from fits of $lnR \propto E_g/2k_BT$ in the 80-300 K range. The BR results from run 1 and run 2 are also displayed for comparison. Pink and blue regions indicated crossover in the response of branching ratio and insulating gap, respectively. The resistance (R) (in logarithmic coordinate) vs $1/T$ Arrhenius plot at several pressures is displayed in the upper corner inset. The inset below shows temperature dependence of the resistance at about 1 Mbar, still exhibiting insulating behavior.

nation of the crossover and mutation operations.[44] Additional exploration of nearby minima was done by distorting and relaxing lowest-enthalpy candidates in the 0-45 GPa pressure range. The dynamical stability of structures was checked with linear response calculations within VASP. As has been determined in previous[45] and the present studies, SOC and magnetic interactions have insignificant effect on the structure stability in sodium iridate compounds. Therefore, all structure searches and phonon calculations were performed without SOC and spin polarization. The analysis of the electronic properties was carried out with SOC and DFT+U corrections[46,47] using $U_{\rm eff} = U - J = 2$ eV value typical for iridates.[48–53] We relied on the U-ramping method[54] starting with $U = 0$ eV and using a 0.2 eV step (runs with 0.1, 0.2, or 0.5 eV steps converged to the same electronic state) to obtain meaningful self-consistent solutions at $U_{\rm eff} = 2$ eV (in what follows we refer to $U_{\rm eff}$ as U for simplicity).

III. RESULTS AND DISCUSSIONS

A. Branching ratio and resistivity measurements

X-ray absorption spectra collected at the Ir $L_{2,3}$ edges are displayed in Fig. 1(a, b) as a function of pressure. In the presence of strong spin-orbit coupling in the $5d$ states (jj coupling), electric dipole transitions ($\Delta j = 0, \pm 1$) at the L_2 edge ($2p_{1/2}$ core level excitation) involve transitions into empty states with $5d_{3/2}$ character, while transitions at the L_3 edge ($2p_{3/2}$ core level excitation) probe empty states with both $5d_{3/2}$ and $5d_{5/2}$ character. On the other hand, in the limit of negligible SOC in the $5d$ states, the ratio of transition probability at L_2 and L_3 edges is only sensitive to the occupation of the ini-

tial core-electron states yielding a "statistical" branching ratio $BR = I_{L3}/I_{L_2} = 2$, where the L_3 "white line" intensity is twice the size of the L_2 "white line". According to theory[55,56], the BR is related to the expectation value of the angular part of the spin-orbit coupling $\langle L \cdot S \rangle$ through $BR = (2+r)/(1-r)$, where $r = \langle L \cdot S \rangle / n_h$ and n_h the average number of $5d$ holes. Figure 1(c) shows the pressure dependence of BR obtained in two independent experimental runs. The measured $BR = 3.8(1)$ at the lowest pressure of 0.3 GPa strongly deviates from the statistical value of 2 and indicates strong spin-orbit interaction present in the $5d$ states. This supports previous findings showing that SOC plays a key role in dictating the electronic structure at ambient pressure[24]. Upon compression, BR increases and peaks at 4.1(1) in the $P \sim 9$ GPa range, decreasing above this pressure. The increase in BR appears to coincide with a concomitant enhancement of the insulating gap with pressure as discussed below. The BR reaches 2.7(2) at $P \sim 52$ GPa. This strong reduction in BR is comparable to that observed in Sr_2IrO_4 at $P \sim 70$ GPa ($BR \sim 2.75$)[32] but stronger than observed in $BaIrO_3$ ($BR \sim 3.3$)[33] and $Sr_3Ir_2O_7$ ($BR \sim 3.0$)[28]. The non-statistical BR indicates that SOC continues to play a role in dictating the electronic ground state even at 50 GPa.

Introducing charge (hole) carriers into the geometrically frustrated Mott insulator $Na_{4-x}Ir_3O_8$ is shown to lead to an anomalous semi-metal state in Na deficient systems ($x = 0.7,\ 1.0$)[24,57]. At ambient pressure (inset of Fig. 2(a)), our $Na_3Ir_3O_8$ single crystal shows poor metallic behavior and a nearly temperature-independent magnetic susceptibility. The paramagnetic and semimetallic properties agree with earlier studies[24]. Figure 2(a) displays electrical resistance versus temperature, $R(T)$, of $Na_3Ir_3O_8$ at selected pressures up to 25 GPa. Pressure-driven insulating behavior clearly emerges already at the lowest measured pressure $P \sim 2$ GPa, indicating a semimetal to insulator transition takes place within this modest pressure range. We note that minimum pressures of $\sim 2-3$ GPa are necessary to obtain low contact resistance in a DAC experiment, so the insulating phase may actually appear at even lower pressures. $R(T)$ curves show non-metallic behavior at all pressures (negative slope). Furthermore, the absolute value of the slope of $R(T)$ becomes larger with increasing pressure up to $P \sim 9$ GPa, indicating that the insulating gap increases with pressure. The low-temperature resistance (~ 2 K) reaches a maximum value of 700 Ω at $P \sim 9$ GPa amounting to an increase of about two orders of magnitude relative to the 7 Ω resistance at $P \sim 2$ GPa. The $R(T)$ plot displayed in the inset of Fig. 2(b) demonstrates that $Na_3Ir_3O_8$ remains an insulator up to at least 1 Mbar. The $R(T)$ data is fitted to a $lnR \propto E_g/(2k_BT)$ dependence in the high temperature range 80-300 K (E_g is the energy gap and k_B is the Boltzmann constant). The exact T-range for the fits is adjusted at each pressure to capture the region where the Arrhenius plot shows a linear dependence; see inset of Fig. 2(b) for representative fits . We note that $R(T)$ cannot be described by a single activation energy over the entire T-range, the low T region below about 80 K deviating from the expected, divergent behavior. The existence of distinct temperature regimes has also been observed in resistance measurements under pressure on Sr_2IrO_4 and $Sr_3Ir_2O_7$ iridates where the high T region is dictated by intrinsic activated transport across the gap while the low T resistance appears to be dominated by extrinsic effects, e.g., creation of sample defects as a result of non-hydrostatic conditions[30].

The main panel of Figure 2(b) displays the fitted values of insulating gap of $Na_3Ir_3O_8$ as a function of pressure, showing a maximum ~ 130 meV at $P \sim 9$ GPa. At higher pressures the energy gap decreases steadily with pressure. The unusual sharp changes in resistance with pressure appear to be correlated with the changes in isotropic BR, as shown in Fig. 2(b).

B. XRD and *ab initio* structure characterization

We now discuss the x-ray powder diffraction measurements under pressure. Diffraction patterns collected at room temperature between 0.6 and 30.6 GPa are displayed in Fig. 3(a). The powder diffraction data collected up to ~ 8.1 GPa could be indexed successfully using the ambient-pressure cubic structure (phase I, space group $P4_132$). Between 8.1 and 11 GPa, new reflections (phase II) start to emerge, signaling a structural phase transition. A sudden change in BR and insulating gap values in the vicinity of $P \sim 9$ GPa accompanies this structural transition. The XRD pattern at $P = 11$ GPa is a mixture of two phases. Further compression results in the complete disappearance of the $P4_132$ reflections. Upon decompression, the signature of phase II disappears below 4.6 GPa, where $Na_3Ir_3O_8$ recovers its ambient cubic structure.

An evolutionary *ab initio* structure search suggests a monoclinic $P2_1$ structure as the ground state for P > 10.5 GPa, as discussed below. A representative Rietveld refinement of the diffraction pattern in the high-pressure phase within this $P2_1$ space group is displayed in Fig. 3(b), corroborating the agreement between theory and experiment.

Ab initio calculations were carried out to identify stable high-pressure phases and aid in the solution of the high pressure crystal structure. The large size of the starting $P4_132$ phase with 56 atoms per primitive unit cell indicated that the structure prediction would present a considerable computational challenge. In fact, confirmed predictions of large-sized high-pressure ground states identified fully 'from scratch', such as the new CaB_6 structure with 28 atoms per primitive unit cell found with an evolutionary algorithm,[44] are still rare. We used a common strategy to accelerate the search by seeding the population with the known ambient-pressure structure but did not rely on any structural or XRD information from the high-pressure measurements to avoid biasing the search towards the experimentally deter-

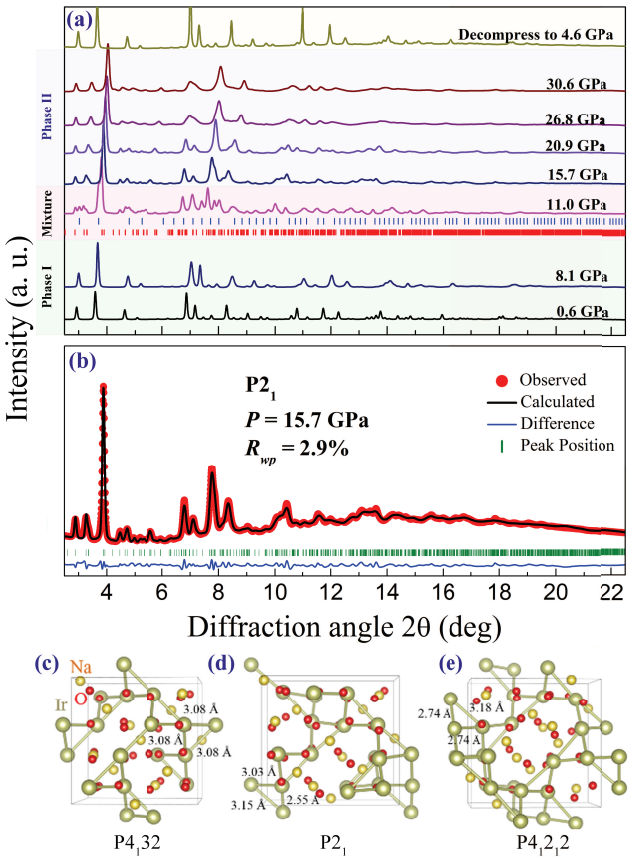

FIG. 3: (a) The background-subtracted diffraction patterns of $Na_3Ir_3O_8$ at high pressures and room temperature. The colored backgrounds represent the changes in the diffraction patterns. A clear structural phase transition takes place above 8.1 GPa where additional peaks appear in the diffraction pattern. The positions of the Bragg reflections of the low pressure (phase I) and high pressure (phase II) phases within the mixture pattern, at the pressure of 11.0 GPa are marked by vertical sticks in blue and red respectively. The structure goes back to ambient pressure phase when pressure is released to 4.6 GPa. (b) Observed and Rietveld refined profiles within space group $P2_1$ at 15.7 GPa (phase II). The solid circles are the experimental data, and black lines for calculated data. The positions of the Bragg reflections are marked by vertical sticks. The blue line represents the residual beneath. (c), (d) (e) Comparison of Ir frameworks in three considered structures fully optimized with DFT at 15 GPa. The lower-symmetry monoclinic phase features unusually short Ir-Ir distances.

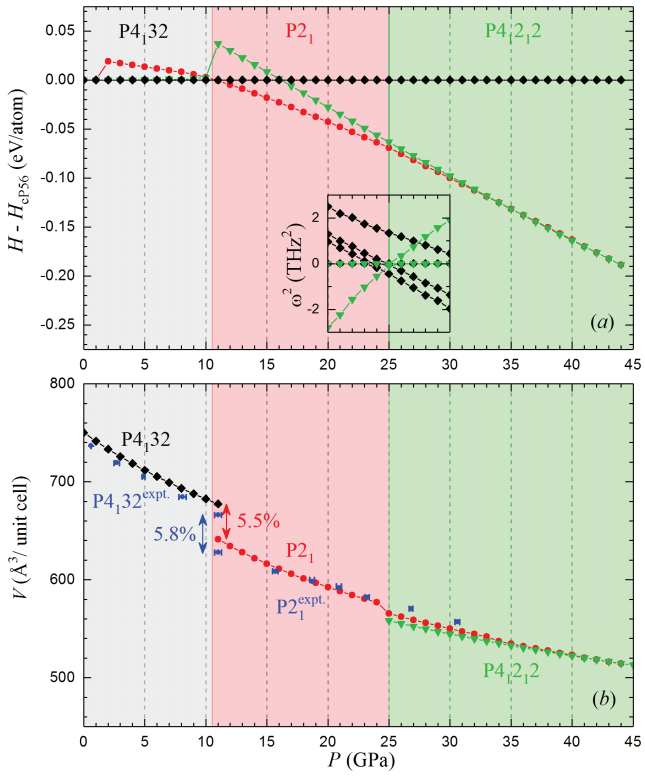

FIG. 4: Relative enthalpy (a) and volume (b) for the ambient cubic $P4_132$ (diamonds), predicted monoclinic $P2_1$ (circles), and predicted $P4_12_12$ (down triangles) phases of $Na_3Ir_3O_8$ under pressure. The top inset shows the frequencies of low-frequency Γ-point phonon modes becoming imaginary above 23 GPa in $P4_132$ and below 25 GPa in $P4_12_12$. The blue circles (with pressure error bars) are the experimental volumes obtained from the XRD data.

mined solution. Surprisingly quickly, a closely matching monoclinic $P2_1$ phase (II) appeared within a 100 local relaxations and remained the lowest-enthalpy in all our evolutionary runs at 15 and 20 GPa. Subsequent finer local optimizations and phonon calculations were performed to determine the range of phase stability and the structural relationship to the starting phase (see Fig. 4(a)). Relaxed at lower pressures, $P2_1$ remained more stable than $P4_132$ down to 10.5 GPa, stayed a local minimum down to 2 GPa, and transformed back to $P4_132$ at ambient pressure. Relaxed at higher pressures, $P2_1$ eventually gained tetragonal $P4_12_12$ symmetry (phase III) above 40 GPa but showed early signs of abrupt structural changes at 25 GPa (Figs. 5). Linear response calculations for the primitive $P4_132$ ($P4_12_12$) unit cells revealed several phonon branches at the Γ point becoming imaginary above 23 GPa (below 25 GPa) which makes the phases dynamically unstable in these pressure ranges. The linear dependence of $\omega^2(P)$ near the transition pressures (Fig. 4(a) inset) indicates soft-mode phase transitions described by Landau theory.[44,58] Table I lists the DFT-optimized structural parameters for the three phases at selected pressures in the corresponding stability ranges.

The calculated 10.5 GPa transition pressure and 5.5% drop in volume for the first-order $P4_132$ to $P2_1$ phase transformation agree well with the corresponding values of 8-11 GPa and 5.8% obtained in our experiment.[59] The collapse of $P4_132$ under pressure could be associated with the lower Na content in the two known stable $Na_3Ir_3O_8$ and $Na_4Ir_3O_8$ compounds with related structures. As has been shown in other materials,[44] metal ions often play a role of 'space fillers' and the insufficient quantity of Na to keep the Ir-O framework 'inflated' in $Na_3Ir_3O_8$ is likely responsible for the quick dynamical

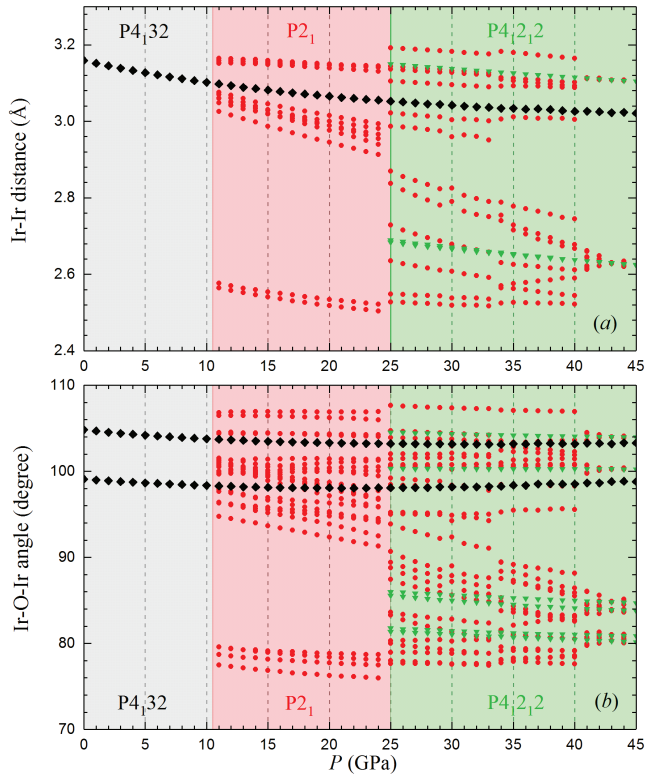

FIG. 5: Calculated dispersion of Ir-Ir distances (a) and Ir-O-Ir angles (b) as a function of pressure in considered $Na_3Ir_3O_8$ phases. Before $P2_1$ gains tetragonal symmetry and transforms into $P4_12_12$ at 40 GPa, it displays abrupt changes and a wide distribution of bonds above 25 GPa.

Phase	Pressure	Space Group	β	a(Å)	b(Å)	c(Å)
Cubic	10 GPa	$P4_132$ (213)		8.8124	8.8124	8.812
	O1 8c (0.1089, 0.1089, 0.1089)		Ir1 12d (0.1250, 0.8775, 0.1275)			
	O2 24e (0.1329, 0.9026, 0.9047)		Na1 8c (0.2513, 0.2513, 0.2513)			
			Na2 4b (0.8750, 0.8750, 0.8750)			
Monoclinic	15 GPa	$P2_1$ (4)	90.081	7.2417	9.5186	8.9662
	O1 2a (0.6173, 0.8915, 0.3887)		O15 2a (0.0969, 0.0960, 0.1243)			
	O2 2a (0.4103, 0.5592, 0.4033)		O16 2a (0.1036, 0.5653, 0.6162)			
	O3 2a (0.9136, 0.4242, 0.0851)		Ir1 2a (0.1066, 0.8802, 0.1293)			
	O4 2a (0.5712, 0.6126, 0.0882)		Ir2 2a (0.3690, 0.6057, 0.6142)			
	O5 2a (0.8981, 0.8565, 0.5711)		Ir3 2a (0.6283, 0.8544, 0.6152)			
	O6 2a (0.3717, 0.9163, 0.1112)		Ir4 2a (0.8486, 0.6295, 0.0983)			
	O7 2a (0.3546, 0.1422, 0.3555)		Ir5 2a (0.3708, 0.1268, 0.1283)			
	O8 2a (0.6383, 0.3153, 0.3863)		Ir6 2a (0.8870, 0.8569, 0.3514)			
	O9 2a (0.8279, 0.8438, 0.1278)		Na1 2a (0.8848, 0.0940, 0.6417)			
	O10 2a (0.1130, 0.6713, 0.1159)		Na2 2a (0.9511, 0.2560, 0.2494)			
	O11 2a (0.6371, 0.1320, 0.1669)		Na3 2a (0.7764, 0.4977, 0.4896)			
	O12 2a (0.1601, 0.8373, 0.3442)		Na4 2a (0.3760, 0.8736, 0.8673)			
	O13 2a (0.3320, 0.3308, 0.1705)		Na5 2a (0.4522, 0.7450, 0.2617)			
	O14 2a (0.8301, 0.6502, 0.3138)		Na6 2a (0.7214, 0.0052, 0.9776)			
Tetragonal	40 GPa	$P4_12_12$ (92)		9.0171	9.0171	6.4229
	O1 8b (0.1362, 0.3911, 0.5858)		Ir1 8b (0.8777, 0.3906, 0.0204)			
	O2 8b (0.1642, 0.0621, 0.6852)		Ir2 4a (0.6496, 0.6496, 0.0000)			
	O3 8b (0.8220, 0.1141, 0.5453)		Na1 4a (0.1167, 0.1167, 0.0000)			
	O4 8b (0.8539, 0.4062, 0.7217)		Na2 8b (0.9994, 0.2232, 0.6641)			

TABLE I: Structural parameters for the three considered phases optimized with the DFT at the specified pressures.

and thermodynamic destabilization of the starting phase under compression. Interestingly, our *ab initio* calculations predict that the high-pressure $P2_1$ is softer than the ambient pressure phase, as indicated by the reduction in theoretical bulk modulus from 88.2 to 57.9 GPa (Fig. 4).[60] Pressure-induced transitions to softer phases are uncommon but have been observed before in materials featuring a loss of symmetry under compression.[61,62] Experimentally, the bulk modulus of the high-pressure phase is found to be 88.2 GPa, higher than 82.7 GPa for the low-pressure phase (all bulk modulus values were obtained from fits of the P-V relation to a second-order Birch-Murnaghan equation). Nevertheless, the agreement between experimental and calculated compressibilities and size of the volume collapse is reasonable good, as shown in Fig. 4(b).

The eventual $P2_1$ to $P4_12_12$ symmetry-gaining transformation predicted with the DFT calculation for pressures above 25 GPa proved to be more difficult to confirm. Although no apparent symmetry change is seen in our experimental diffraction patterns up to 30.6 GPa, substantially broadened and merged diffraction peaks are observed in our patterns at and above 26.8 GPa which may be indicative of proximity to a second structural phase transition. Extending the XRD measurements and unconstrained structure searches to higher pressure is needed to explore the possible existence of other stable phase(s). As a test of systematic DFT errors, we repeated the full set of calculations shown in Fig. 4 in the local density approximation (LDA) and observed a typical degree of agreement between the LDA and GGA flavors, with the former tending to overstabilize more compact structures.[63,64] Namely, the $P4_132$ to $P2_1$ transition occurred at 8.0 GPa with a 4.9% drop in volume and a change in bulk modulus from 102.5 to 70.3 GPa while the dynamical destabilization of $P4_132$ and $P4_12_12$ was observed above 14 GPa and below 20 GPa, respectively.

Examination of the atomic environments in the three phases optimized with DFT uncovers a dramatic rearrangement in the Ir framework under compression. Fig. 3(c-e) and Fig. 5(a) show that the Ir backbone in the ambient pressure $P4_132$ phase consists of equilateral Ir triangles. These become distorted in the $P2_1$ phase to an extent that one side of some Ir_3 units collapses from 3.08 Å down to 2.55 Å. For comparison, two sides of the Ir triangles shorten to 2.74 Å in the metastable $P4_12_12$ phase at 15 GPa. Considering that the nearest neighbor distance in metallic fcc-Ir at 15 GPa is 2.71 Å, the direct Ir-Ir interactions and possible bonding are clearly far more important in the high-pressure lower-symmetry phases compared to those in the cubic $P4_132$ phase. Another notable structural change that must have an effect on the compound's electronic properties is the appearance of a wide dispersion of Ir-O-Ir angles, some of which as low as 76 degrees (Fig. 5(b)).

C. Electronic structure theory and experiment

Accurate modeling of the iridate's electronic behavior requires the inclusion of both SOC and electronic correlation due to the comparable magnitudes of these effects in $5d$ transition metal oxides. We found the SOC to induce only minor changes in the crystal structure parameters or the relative stability for the studied $Na_3Ir_3O_8$ phases.[65] In contrast, it had a pronounced impact on the electronic structure, e.g., transforming $P4_132$ at 0 GPa from a band insulator into a semimetal in agreement with previously reported DFT results.[24] Combining the fully relativistic simulations with an advanced treatment of the electronic correlation, e.g., with GW or hybrid functionals, is presently not feasible due to the large system size and we relied on the more affordable DFT+U method. The approach has been widely used to model iridates[48–53] but it is important to note that the $U \sim 2$ eV values meaningful for $5d$ oxides are not always sufficient to reproduce the experimentally observed semiconducting behavior.[50] In some cases, the failure of DFT+U to open up a band gap was attributed to U being applied only to the $5d$ orbitals rather than the $5d-2p$ hybrids and corrected with Wannier functions.[66] Our tests uncovered another issue related to the appearance of multiple self-consistent-field (scf) electronic configuration minima in DFT+U simulations. Direct calculations with the desired (large) U values tend to get stuck in local minima and the problem can oftentimes be solved by gradually increasing the U value in small steps starting from 0 eV, a procedure known as U-ramping.[54] Surprisingly, our direct calculations with $U = 2$ eV converged to noticeably *lower*-enthalpy self-consistent minima compared to the U-ramping runs. Moreover, we noticed that if the charge density and wavefunctions from a scf U-ramping calculation were used to initialize a non-scf calculation as a test of convergence reproducibility, the non-scf run consistently produced a different electronic solution with noticeably higher enthalpy (an outcome we have not encountered in the DFT calculations without U). For example, the three distinct minima obtained for $U = 2$ eV in the direct, U-ramping, and follow-up non-scf calculations had the following enthalpies referenced to the U-ramping case: -4 meV/atom, 0 meV/atom, +16 meV/atom for $P4_132$ at 10 GPa and -2 meV/atom, 0 meV/atom, +15 meV/atom for $P2_1$ at 10 GPa. Despite being enthalpically favored, the electronic minima obtained in the direct runs turned out to have unphysically dispersed bands and a high DOS at the Fermi level. The minima obtained in the scf U-ramping calculations were also found to have an unphysical DOS with a reduced pseudogap compared to that in the $U = 0$ eV calculations. The non-scf calculations initialized with the scf U-ramping charge density and wavefunctions produced the most reasonable DOS and band structure results shown in Figs. 6 and 7 but should be taken with a grain of salt. A more systematic exploration of the electronic configuration space, e.g., with the help of occupation matrices,[67,68] will require a considerable computational effort for systems of the considered size.

Fig. 6 demonstrates that the semimetallicity in $P4_132$ at ambient pressure is defined by the nearly free electron 3D states centered at the R k-point. The inclusion of U

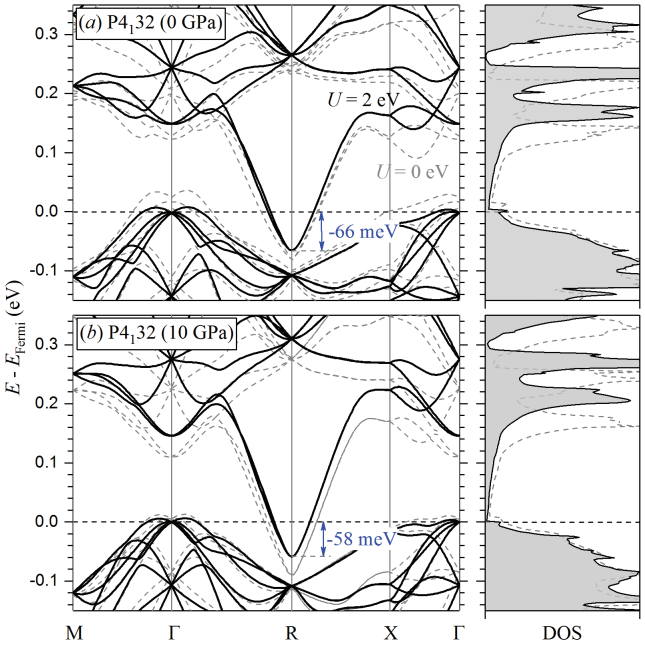

FIG. 6: Band structures and DOS calculated for $P4_132$ at 0 and 10 GPa. The black solid lines correspond to the results for $U = 2$ eV values ramped up with a 0.2 eV step while the gray dashed lines denote the results for $U = 0$.

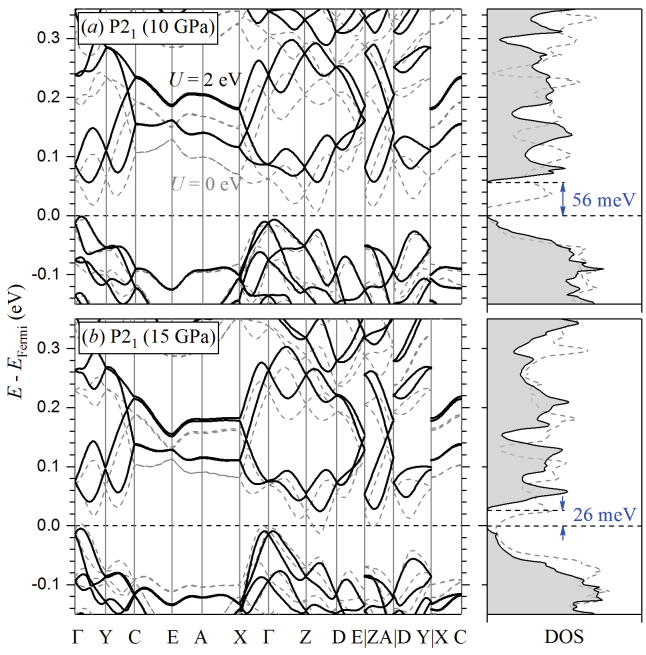

FIG. 7: Band structure and DOS calculated for $P2_1$ at 10 and 15 GPa. The U settings are the same as in Fig. 6. Due to the small deviation of β from 90 degrees some high-symmetry directions in the Brillouin zone are omitted.

raises the relative position of this band by about 50 meV and leaves it 66 meV below the Fermi level. We observe that the DFT+U treatment of the correlation does not open up a band gap in $P4_132$ under compression, as the bottom of the band at the R point shows only a minor upshift. We checked that the phase remains semimetallic if either U is ramped up to 4 eV or the pressure is increased up to 45 GPa. Fig. 7 shows that immediately after the transformation the $P2_1$ phase does display a band gap of 56 meV which is comparable to the values extracted from the experiment. However, the calculated band gap closes quickly with pressure which makes both $P2_1$ and $P4_12_12$ phases metallic above 25 GPa. We conclude that DFT+U correctly predicts the pressure-induced trends in the band separation near the Fermi level (an increase for $P4_132$ and a decrease for $P2_1$) but cannot quantitatively resolve the small band gap values in this material. We note that the evolution of the bandwidth of the 5d manifold that dominates the density of states at the Fermi level (with bottom and top edges around -1.5 and +1.0 eV, respectively) is consistent with the calculated response of the iridium framework to compression. Namely, the bandwidth increases only slightly from 2.21 eV (0 GPa) to 2.26 eV (10 GPa) within the $P4_132$ structure but jumps to 2.66 eV (10 GPa) and 2.83 eV (15 GPa) after the transformation into the $P2_1$ phase.

We now turn to the interplay between electronic (SOC, insulating gap) and structural responses to pressure. The subtle interplay between structural and electronic degrees of freedom has been addressed in previous studies of iridates. For example, in the Mott-insulator Sr_2IrO_4 electron hopping is predicted to strongly depend on Ir-O-Ir bond angle,[69–71] with a change $\Delta\theta \sim 13°$ being necessary to close the $\sim$ 100 meV Mott gap.[72] A pressure-driven enhancement of the insulating gap has been reported in $BaIrO_3$.[33] Additionally, the metallic phase of $BaIrO_3$ obtained by rare-earth element doping can be driven back into the insulating state with modest pressures of $P \sim 1$ GPa. The reentrant insulating state in $BaIrO_3$ was attributed to a decrease in Ir-O-Ir bond angle away from collinear configuration.[70] While our XRD data does not allow precise refinement of oxygen positions in the unit cell as a result of the weak scattering power of these low-Z atoms, we can obtain insight into the structural distortions from the DFT calculations which correctly predict the $P \sim 10$ GPa transition as validated by experiment. Figure 5(b) shows a decrease with pressure in Ir-O-Ir bond angle in the low-pressure phase (phase I). This is expected to suppress $t_{pd\pi}$ electron hopping between nearest neighbor Ir 5d orbitals via oxygen p orbitals .[24] This structural modification may contribute to the semimetal-to-insulator transition as well as the continued enhancement of insulating gap in the low-pressure phase. The reduction of bonding angle in the low-pressure phase, however, is only about 1.5 degrees which seems small in order to explain the very large gap change by $\sim$ 90 meV from 2.1 GPa to 9 GPa. While a pressure-induced insulating state in transition metal oxides may be counterintuitive, this is not uncommon as changes in electron hopping as a result of lattice distortions (bond angles, hybridization), high-spin to low-spin transition (d-orbital occupancy), and exchange (magnetic) interactions can lead to insulating states.[33,70,73,74] In $Na_3Ir_3O_8$, the number of average d electrons per Ir atom is non-integer, 4.67 ($Ir^{4.33+}$), and the 5d electrons are all accommodated into the t_{2g} manifold because of the large $t_{2g} - e_g$ crystal electric field splitting 10Dq $\sim$ 4 eV. Although $Na_3Ir_3O_8$ is paramagnetic (PM) at ambient pressure (Fig. 2 (a)), the exact nature of the magnetic ground state at high pressure remains elusive.

The sum of integrated $L_{2,3}$ intensity in isotropic XAS spectra is proportional to the number of 5d holes.[75] The pressure dependence of the sum of $L_{2,3}$ intensity for two independent experimental runs is displayed in the inset of Fig. 1(c). The 5d hole (electron) occupation shows an overall incremental decrease (increase) with pressure, with a total change of $\sim$ 7% at 52 GPa. The majority of the change is observed below about 10 GPa, namely, within the low-pressure phase. We note that the limited number of data points below about 4 GPa, together with a small relative change in hole count to this pressure, prevents us from assigning significance to the apparent increase in hole count below about 4 GPa. A possible explanation for the overall decrease in hole count is charge-transfer from the oxygen 2p ligands due to the reduction in Ir-O bond length with pressure (for example in $Na_4Ir_3O_8$ the t_{2g} complex is composed of 70% Ir 5d character, 20% O_2 2p character, and 4% O_1 2p character at ambient pressure). Shortened bond lengths enhance hybridization and electron hopping between O and Ir. However, increased electron occupation on the Ir site and decreased bonding angle will act to reduce electron hopping as a result of increased Coulomb interactions and reduced bandwidth. For example the half-filled $J_{\text{eff}} = 1/2$ state is gapped by even a small on-site Coulomb repulsion (U) in the presence of strong SOC.[17,18] At ambient pressure, $Na_3Ir_3O_8$ has a 1/3-filled $J_{\text{eff}} = 1/2$ state. As the number of holes (electrons) decreases (increases), the less than half-filled $J_{\text{eff}} = 1/2$ band (hole-doped semimetal) moves towards a half-filled $J_{\text{eff}} = 1/2$ state stabilizing a Mott state in the presence of SOC. Since SOC remains robust even at highest pressures, U plays a more important role in gap formation as pressure increases as a result of the increase in 5d electron occupation (a near 10% change in electron occupation translates to nearly 0.5 electron which brings the system to the verge of half-filled $J_{\text{eff}} = 1/2$ state). It is interesting to note that the magnitude of the insulating gap reaches about 130 meV in the low-pressure phase which is not much different than what is found in other iridates near half-filling. The reduction in Ir-O-Ir bond angle together with the decrease in hole count and related move towards half-filling of the $J_{\text{eff}} = 1/2$ states are likely to play the leading role in dictating the evolution of insulating gap size in the low-pressure phase.

The increased electron occupancy on Ir 5d states pri-

marily takes place in the low-pressure range below the structural transition (inset of Fig. 1(c)). If the nominal Ir valence moves from 4.33^+ towards 4^+ one would expect a reduction in isotropic BR since more electrons in $J_{\text{eff}} = 1/2$ states, only accessible at the L_3 edge, would decrease the absorption cross section at this edge more than that at the L_2 edge. This seems to contradict the experimental result that the BR increases from ambient to $\sim$ 9 GPa. However, an increase in electron occupancy and reduction in Ir-O-Ir bond angle drive the system more insulating in the low-pressure phase. The more localized state results in reduced electron hopping and bandwidth as well as a reduced admixture of J_{eff} states, which enhances the BR even without a change in the strength of SOC. This is consistent with insight from DFT calculations of ruthenates and iridates where an increase in Hubbard U results in a decrease in admixture of J_{eff} states, namely, an apparent increase in the effective SOC.[76,77] The increasing BR at low pressure is a manifestation of this increased localization. One can then understand the sharp, correlated decrease in insulating gap and BR above the structural phase transition based on the same arguments. The lower-symmetry monoclinic $P2_1$ structure features a distorted Ir framework with remarkably short Ir-Ir distances comparable to those in fcc-Ir at 15 GPa (2.71 Å). While the number of holes is roughly constant above the structural phase transition at 10 GPa ($\sim$ 1% decrease from 10 to 50 GPa), the volume collapse and dimerization of some of the Ir bonds in the high-pressure phase will introduce sizable increases in electronic bandwidth leading to a reduction in insulating gap above the transition. Further compression leads to additional increases in bandwidth and a further continuous reduction in insulating gap. The reversal in the pressure-dependence of the insulating gap at $\sim$ 9 GPa is clearly a consequence of the structural phase transition. The reduction in BR in the high-pressure phase is likely to originate in bandwidth-driven mixing of $J_{\text{eff}} = 1/2$, 3/2 states, with the influence of SOC becoming less prominent in dictating the electronic ground state at high pressure. Despite the apparent dimerization and strong reduction in electronic gap, the system remains insulating to the highest measured pressure likely a result of wide distribution of Ir-O-Ir bond angles including some below 80 degrees (Fig. 5(b)). Clearly, the attained maximum pressure of 1 Mbar is not sufficient to close the gap completely (inset of Fig. 2(b)), indicating that higher pressures are necessary to drive the system into a metallic state.

IV. CONCLUSION

A semimetal-to-insulator transition is observed in $Na_3Ir_3O_8$ with application of a modest pressure of $\sim$ 2 GPa. The insulating gap increases with pressure in the low-pressure, cubic phase up to 9 GPa where a first-order structural phase transition featuring Ir-Ir dimerization drives a reduction in insulating gap which continues to decrease upon compression in the high-pressure phase. The isotropic BR maps the response of the insulating gap to pressure indicating that degree of localization goes hand in hand with admixture of J_{eff} states. A reduction in Ir-O-Ir bond angle together with an overall increase in electron occupation in the low-pressure phase, moving the $J_{\text{eff}} = 1/2$ states towards half-filling, appears to be the leading cause for the enhancement of the insulating gap in the low-pressure phase. Near half-filling U plays a more dominant role in gap formation in the presence of robust SOC. The high-pressure structure above 10 GPa features a distorted Ir framework with unusually short bond lengths which accounts for the reduced insulating gap although a broad distribution of Ir-O-Ir bond angles may prevent the system from becoming metallic even at $\sim$ 1 Mbar. Since pressure usually enhances orbital overlap and bandwidth, a pressure-induced insulating state is not commonplace. The emergence of a pressure-induced robust insulating state within the cubic phase of $Na_3Ir_3O_8$ indicates that pressure provides a unique route to manipulate the delicate balance between SOC, bandwidth, Coulomb repulsion, and crystal field interactions in this material.

V. ACKNOWLEDGEMENT

Work at HPSTAR is supported by NSFC under Grants No.51527801 and No. U1530402. Work at APS was supported by the U.S. Department of Energy (DOE), Office of Science, under Contract No. DE-AC02-06CH11357. Work at Institute of Physics Chinese Academy of Sciences (IOPCAS) is supported by National Natural Science Foundation of China (NSFC) and Ministry of Science & Technology (MOST) of China through Research Projects, as well as by CAS External Cooperation Program of Bureau of International Cooperation (BIC) (Grant No. 112111KYS820150017). E.D.S. and A.N.K. acknowledge the NSF support (Award No. DMR-1410514). H.K.M and W.Y. acknowledge the financial support from DOE-BES X-ray Scattering Core Program under Grant No. DE-FG02-99ER45775. HPCAT operations are supported by the U.S. DOE National Nuclear Security Administration (NNSA) under Award No. DE-NA0001974 and DOE Basic Energy Sciences (BES) under Award No.DE-FG02-99ER45775, with partial instrumentation funding by National Science Foundation (NSF). Work in the Materials Science Division of Argonne National Laboratory (crystal synthesis, magnetic and transport measurements) was supported by the U.S. Department of Energy, Office of Science, Basic Energy Sciences, Materials Science and Engineering Division. F. Sun acknowledges useful discussions with Yang Ding.

* Electronic address: kolmogorov@binghamton.edu
† Electronic address: haskel@aps.anl.gov

[1] J. G. Bednorz and K. A. Müller, Zeitschrift für Physik B Condensed Matter **64**, 189 (1986), ISSN 1431-584X, URL https://doi.org/10.1007/BF01303701.
[2] B. Keimer, S. A. Kivelson, M. R. Norman, S. Uchida, and J. Zaanen, NATURE **518**, 179 (2015).
[3] Y. Kamihara, T. Watanabe, M. Hirano, and H. Hosono, Journal of the American Chemical Society **130**, 3296 (2008), pMID: 18293989, https://doi.org/10.1021/ja800073m, URL https://doi.org/10.1021/ja800073m.
[4] G. R. Stewart, Rev. Mod. Phys. **83**, 1589 (2011), URL https://link.aps.org/doi/10.1103/RevModPhys.83.1589.
[5] D. B. McWhan and T. M. Rice, Phys. Rev. Lett. **22**, 887 (1969), URL https://link.aps.org/doi/10.1103/PhysRevLett.22.887.
[6] H. Kato, T. Okuda, Y. Okimoto, Y. Tomioka, K. Oikawa, T. Kamiyama, and Y. Tokura, Phys. Rev. B **65**, 144404 (2002), URL https://link.aps.org/doi/10.1103/PhysRevB.65.144404.
[7] A.Poddar and S.Das, Physica B: Condensed Matter **344**, 325 (2004), ISSN 0921-4526, URL http://www.sciencedirect.com/science/article/pii/S0921452603009608.
[8] R. Ramesh and N. A. Spaldin, NATURE MATERIALS **6**, 21 (2007), ISSN 1476-1122.
[9] C. Rao, Annual Review of Physical Chemistry **40**, 291 (1989), https://doi.org/10.1146/annurev.pc.40.100189.001451, URL https://doi.org/10.1146/annurev.pc.40.100189.001451.
[10] M. Imada, A. Fujimori, and Y. Tokura, Rev. Mod. Phys. **70**, 1039 (1998), URL https://link.aps.org/doi/10.1103/RevModPhys.70.1039.
[11] Y. Tokura and N. Nagaosa, Science **288**, 462 (2000), ISSN 0036-8075, http://science.sciencemag.org/content/288/5465/462.full.pdf, URL http://science.sciencemag.org/content/288/5465/462.
[12] E. Dagotto, Science **309**, 257 (2005), ISSN 0036-8075, http://science.sciencemag.org/content/309/5732/257.full.pdf, URL http://science.sciencemag.org/content/309/5732/257.
[13] J. Zhang and R. Averitt, Annual Review of Materials Research **44**, 19 (2014), https://doi.org/10.1146/annurev-matsci-070813-113258, URL https://doi.org/10.1146/annurev-matsci-070813-113258.
[14] M. W. Haverkort, I. S. Elfimov, L. H. Tjeng, G. A. Sawatzky, and A. Damascelli, Phys. Rev. Lett. **101**, 026406 (2008), URL https://link.aps.org/doi/10.1103/PhysRevLett.101.026406.
[15] L. Balents, NATURE **464**, 199 (2010), ISSN 0028-0836.
[16] D. Pesin and L. Balents, NATURE PHYSICS **6**, 376 (2010), ISSN 1745-2473.
[17] B. J. Kim, H. Jin, S. J. Moon, J.-Y. Kim, B.-G. Park, C. S. Leem, J. Yu, T. W. Noh, C. Kim, S.-J. Oh, et al., Phys. Rev. Lett. **101**, 076402 (2008), URL https://link.aps.org/doi/10.1103/PhysRevLett.101.076402.
[18] B. J. Kim, H. Ohsumi, T. Komesu, S. Sakai, T. Morita, H. Takagi, and T. Arima, SCIENCE **323**, 1329 (2009), ISSN 0036-8075.
[19] Y. Singh and P. Gegenwart, Phys. Rev. B **82**, 064412 (2010), URL https://link.aps.org/doi/10.1103/PhysRevB.82.064412.
[20] J. c. v. Chaloupka, G. Jackeli, and G. Khaliullin, Phys. Rev. Lett. **110**, 097204 (2013), URL https://link.aps.org/doi/10.1103/PhysRevLett.110.097204.
[21] Y. Okamoto, M. Nohara, H. Aruga-Katori, and H. Takagi, Phys. Rev. Lett. **99**, 137207 (2007), URL https://link.aps.org/doi/10.1103/PhysRevLett.99.137207.
[22] W. Witczak-Krempa, G. Chen, Y. B. Kim, and L. Balents, Annual Review of Condensed Matter Physics **5**, 57 (2014), https://doi.org/10.1146/annurev-conmatphys-020911-125138, URL https://doi.org/10.1146/annurev-conmatphys-020911-125138.
[23] R. Dally, T. Hogan, A. Amato, H. Luetkens, C. Baines, J. Rodriguez-Rivera, M. J. Graf, and S. D. Wilson, Phys. Rev. Lett. **113**, 247601 (2014), URL https://link.aps.org/doi/10.1103/PhysRevLett.113.247601.
[24] T. Takayama, A. Yaresko, A. Matsumoto, J. Nuss, K. Ishii, M. Yoshida, J. Mizuki, and H. Takagi, SCIENTIFIC REPORTS **4**, 6818 (2014), ISSN 2045-2322.
[25] V. Hermann, J. Ebad-Allah, F. Freund, I. Pietsch, A. Jesche, A. A. Tsirlin, J. Deisenhofer, M. Hanfland, P. Gegenwart, and C. A. Kuntscher, Phys. Rev. B **96**, 195137 (2017).
[26] L. Veiga, M. Etter, K. Glazyrin, F. Sun, C. E. Jr., G. Fabbris, J. Mardegan, P. S. Malavi, Y. Deng, P. P. Stavroupoulos, et al., Phys. Rev. B **96**, 140402 (2017).
[27] V. Hermann, M. Altmeyer, J. Ebad-Allah, F. Freund, A. Jesche, A. A. Tsirlin, M. Hanfland, P. Gegenwart, I. I. Mazin, D. I. Khomskii, et al., Phys. Rev. B **97**, 020104 (2018).
[28] C. Donnerer, M. M. Sala, S. Pascarelli, A. D. Rosa, S. N. Andreev, V. V. Mazurenko, T. Irifune, E. C. Hunter, R. S. Perry, and D. F. McMorrow, Phys. Rev. B **97**, 035106 (2018).
[29] Z. Zhao, S. Wang, T. F. Qi, Q. Zheng, S. Hirai, P. P. Konk, L. Li, C. Park, S. J. Yuan, C. Q. Jin, et al., J. Phys.:Condens. Matter **26**, 215402 (2014).
[30] D. Zocco, J. J. Hamlin, B. D. White, B. J. Kim, J. R. Jeffries, S. T. Weir, Y. K. Vohra, J. W. Allen, and M. B. Maple, J. Phys.:Condens. Matter **26**, 255603 (2014).
[31] Y. Ding, L. Yang, C.-C. Chen, H.-S. Kim, M. J. Han, W. Luo, Z. Feng, M. Upton, D. Casa, J. Kim, et al., Phys. Rev. Lett. **116**, 216402 (2016), URL https://link.aps.org/doi/10.1103/PhysRevLett.116.216402.
[32] D. Haskel, G. Fabbris, M. Zhernenkov, P. P. Kong, C. Q. Jin, G. Cao, and M. van Veenendaal, Phys. Rev. Lett. **109**, 027204 (2012), URL https://link.aps.org/doi/10.1103/PhysRevLett.109.027204.
[33] M. A. Laguna-Marco, G. Fabbris, N. M. Souza-Neto, S. Chikara, J. S. Schilling, G. Cao, and D. Haskel, Phys. Rev. B **90**,

014419 (2014), URL https://link.aps.org/doi/10.1103/PhysRevB.90.014419.
[34] H. Zheng, J. Zhang, C. C. Stoumpos, Y. Ren, Y.-S. Chen, R. Dally, S. D. Wilson, Z. Islam, and J. F. Mitchell, Phys. Rev. Mat. **2**, 043403 (2018).
[35] D. Haskel, Y. C. Tseng, J. C. Lang, and S. Sinogeikin, REVIEW OF SCIENTIFIC INSTRUMENTS **78**, 083904 (2007), ISSN 0034-6748.
[36] P. P. Kong, F. Sun, L. Y. Xing, J. Zhu, S. J. Zhang, W. M. Li, Q. Q. Liu, X. C. Wang, S. M. Feng, X. H. Yu, et al., SCIENTIFIC REPORTS **4**, 6679 (2014), ISSN 2045-2322.
[37] G. Kresse and J. Hafner, Phys. Rev. B **47**, 558 (1993).
[38] G. Kresse and J. Furthmüller, Phys. Rev. B **54**, 11169 (1996).
[39] P. Blöchl, Phys. Rev. B **50**, 17953 (1994).
[40] J. P. Perdew, K. Burke, and M. Ernzerhof, Phys. Rev. Lett. **77**, 3865 (1996).
[41] J. Perdew, K. Burke, and M. Ernzerhof, Phys. Rev. Lett. **78**, 1396 (1997).
[42] J. D. Pack and H. J. Monkhorst, Phys. Rev. B **13**, 5188 (1976).
[43] J. D. Pack and H. J. Monkhorst, Phys. Rev. B **16**, 1748 (1977).
[44] A. N. Kolmogorov, S. Shah, E. R. Margine, A. K. Kleppe, and A. P. Jephcoat, Phys. Rev. Lett. **109**, 075501 (2012), URL https://link.aps.org/doi/10.1103/PhysRevLett.109.075501.
[45] S. K. Choi, R. Coldea, A. N. Kolmogorov, T. Lancaster, I. I. Mazin, S. J. Blundell, P. G. Radaelli, Y. Singh, P. Gegenwart, K. R. Choi, et al., Phys. Rev. Lett. **108**, 127204 (2012), URL https://link.aps.org/doi/10.1103/PhysRevLett.108.127204.
[46] A. I. Liechtenstein, V. I. Anisimov, and J. Zaanen, Phys. Rev. B **52**, R5467 (1995), URL https://link.aps.org/doi/10.1103/PhysRevB.52.R5467.
[47] S. L. Dudarev, G. A. Botton, S. Y. Savrasov, C. J. Humphreys, and A. P. Sutton, Phys. Rev. B **57**, 1505 (1998), URL https://link.aps.org/doi/10.1103/PhysRevB.57.1505.
[48] S. J. Moon, H. Jin, K. W. Kim, W. S. Choi, Y. S. Lee, J. Yu, G. Cao, A. Sumi, H. Funakubo, C. Bernhard, et al., Phys. Rev. Lett. **101**, 226402 (2008), URL https://link.aps.org/doi/10.1103/PhysRevLett.101.226402.
[49] M. A. Zeb and H.-Y. Kee, Phys. Rev. B **86**, 085149 (2012), URL https://link.aps.org/doi/10.1103/PhysRevB.86.085149.
[50] Y. Okada, D. Walkup, H. Lin, C. Dhital, T.-R. Chang, S. Khadka, W. Zhou, H.-T. Jeng, M. Paranjape, A. Bansil, et al., Nature Materials **12**, 707 (2013), URL http://dx.doi.org/10.1038/nmat3653.
[51] K. Foyevtsova, H. O. Jeschke, I. I. Mazin, D. I. Khomskii, and R. Valentí, Phys. Rev. B **88**, 035107 (2013), URL https://link.aps.org/doi/10.1103/PhysRevB.88.035107.
[52] H.-S. Kim, Y. Chen, and H.-Y. Kee, Phys. Rev. B **91**, 235103 (2015), URL https://link.aps.org/doi/10.1103/PhysRevB.91.235103.
[53] V. Hermann, J. Ebad-Allah, F. Freund, I. M. Pietsch, A. Jesche, A. A. Tsirlin, J. Deisenhofer, M. Hanfland, P. Gegenwart, and C. A. Kuntscher, Phys. Rev. B **96**, 195137 (2017), URL https://link.aps.org/doi/10.1103/PhysRevB.96.195137.
[54] B. Meredig, A. Thompson, H. A. Hansen, C. Wolverton, and A. van de Walle, Phys. Rev. B **82**, 195128 (2010), URL https://link.aps.org/doi/10.1103/PhysRevB.82.195128.
[55] G. van der Laan and B. T. Thole, Phys. Rev. Lett. **60**, 1977 (1988), URL https://link.aps.org/doi/10.1103/PhysRevLett.60.1977.
[56] B. T. Thole and G. van der Laan, Phys. Rev. A **38**, 1943 (1988), URL https://link.aps.org/doi/10.1103/PhysRevA.38.1943.
[57] A. Balodhi, A. Thamizhavel, and Y. Singh, Phys. Rev. B **91**, 224409 (2015), URL https://link.aps.org/doi/10.1103/PhysRevB.91.224409.
[58] Y. Xu, L. Zhang, T. Cui, Y. Li, Y. Xie, W. Yu, Y. Ma, and G. Zou, Phys. Rev. B **76**, 214103 (2007), URL https://link.aps.org/doi/10.1103/PhysRevB.76.214103.
[59] The transition pressure value found in the DFT calculations at zero temperature may shift by a few GPa if the finite-temperature contribution due to vibrational entropy is taken into account.
[60] Our additional searches for possible nearby minima with more conventional response to pressure indicated that the originally determined $P2_1$ is the lowest-enthalpy structure in the 11-25 GPa range, at least for unit cells up to 56 atoms. In particular, we (i) followed the eigenvectors of imaginary phonon modes in $P4_132$ and $P4_12_12$; (ii) finely relaxed dozens of randomized $P2_1$ structures with and without the $P2_1$ symmetry constraint at different pressures; and (iii) calculated Γ-point phonons for $P2_1$ at 15 GPa.
[61] J. Haines, J. Leger, and O. Schulte, JOURNAL OF PHYSICS-CONDENSED MATTER **8**, 1631 (1996), ISSN 0953-8984.
[62] F. Rivadulla, M. Banobre-Lopez, C. X. Quintela, A. Pineiro, V. Pardo, D. Baldomir, M. Arturo Lopez-Quintela, J. Rivas, C. A. Ramos, H. Salva, et al., NATURE MATERIALS **8**, 947 (2009).
[63] A. N. Kolmogorov, S. Hajinazar, C. Angyal, V. L. Kuznetsov, and A. P. Jephcoat, Phys. Rev. B **92**, 144110 (2015), URL https://link.aps.org/doi/10.1103/PhysRevB.92.144110.
[64] C. Fan, C. Liu, F. Peng, N. Tan, M. Tang, Q. Zhang, Q. Wang, F. Li, J. Wang, Y. Chen, et al., Physica B: Condensed Matter **521**, 6 (2017), ISSN 0921-4526, URL http://www.sciencedirect.com/science/article/pii/S0921452617303289.
[65] At 20 GPa the relative enthalpy for mP56 (tP56) was 43 meV/atom (28 meV/atom) without SOC (see Fig. 1) and 38 meV/atom (18 meV/atom) with SOC while the shortest Ir-Ir distances remained within 0.7% in the two treatments. For DOS and band structure calculations we used a $8 \times 8 \times 8$ k-mesh and relaxed the unit cells with SOC.
[66] K.-W. Lee and W. E. Pickett, Europhysics Letters **80**, 37008 (2007), URL http://stacks.iop.org/0295-5075/80/i=3/a=37008.
[67] J. P. Allen and G. W. Watson, Phys. Chem. Chem. Phys. **16**, 21016 (2014), URL http://dx.doi.org/10.1039/C4CP01083C.
[68] B. Dorado, B. Amadon, M. Freyss, and M. Bertolus, Phys. Rev. B **79**, 235125 (2009).

[69] S. Chikara, O. Korneta, W. P. Crummett, L. E. DeLong, P. Schlottmann, and G. Cao, Phys. Rev. B **80**, 140407 (2009), URL https://link.aps.org/doi/10.1103/PhysRevB.80.140407.
[70] O. B. Korneta, T. Qi, S. Chikara, S. Parkin, L. E. De Long, P. Schlottmann, and G. Cao, Phys. Rev. B **82**, 115117 (2010), URL https://link.aps.org/doi/10.1103/PhysRevB.82.115117.
[71] M. Ge, T. F. Qi, O. B. Korneta, D. E. De Long, P. Schlottmann, W. P. Crummett, and G. Cao, Phys. Rev. B **84**, 100402 (2011), URL https://link.aps.org/doi/10.1103/PhysRevB.84.100402.
[72] S. J. Moon, H. Jin, W. S. Choi, J. S. Lee, S. S. A. Seo, J. Yu, G. Cao, T. W. Noh, and Y. S. Lee, Phys. Rev. B **80**, 195110 (2009), URL https://link.aps.org/doi/10.1103/PhysRevB.80.195110.
[73] T. Matsuoka and K. Shimizu, NATURE **458**, 186 (2009), ISSN 0028-0836.
[74] R. Lengsdorf, M. Ait-Tahar, S. S. Saxena, M. Ellerby, D. I. Khomskii, H. Micklitz, T. Lorenz, and M. M. Abd-Elmeguid, Phys. Rev. B **69**, 140403 (2004), URL https://link.aps.org/doi/10.1103/PhysRevB.69.140403.
[75] J. Stöhr, Journal of Magnetism and Magnetic Materials **200**, 470 (1999), ISSN 0304-8853, URL http://www.sciencedirect.com/science/article/pii/S0304885399004072.
[76] H.-S. Kim, V. S. V., A. Catuneanu, and H.-Y. Kee, Phys. Rev. B **91**, 241110 (2015), URL https://link.aps.org/doi/10.1103/PhysRevB.91.241110.
[77] H.-S. Kim, E. K.-H. Lee, and Y. B. Kim, EPL (Europhysics Letters) **112**, 67004 (2015), URL http://stacks.iop.org/0295-5075/112/i=6/a=67004.